RESEARCH PAPER

MR-u: Material Characterization Using 3D Displacement-Encoded Magnetic Resonance and the Virtual Fields Method

J.B. Estrada[1] · C.M. Luetkemeyer[1] · U.M. Scheven[1] · E.M. Arruda[1,2,3]

Abstract

Background Experimental, fully three-dimensional mechanical characterization of opaque materials with arbitrary geometries undergoing finite deformations is generally challenging.

Objective We present a promising experimental method and processing pipeline for acquiring and processing full-field displacements and using them toward inverse characterization using the Virtual Fields Method (VFM), a combination we term MR-***u***.

Methods Silicone of varying crosslinker concentrations and geometries is used as the sample platform. Samples are stretched cyclically to finite deformations inside a 7T MRI machine. Synchronously, a custom MRI pulse sequence encodes the local displacement in the phase of the MR image. Numerical differentiation of phase maps yields strains.

Results We present a custom image processing scheme for this numerical differentiation of MRI phase-fields akin to convolution kernels, as well as considerations for gradient set calibration for data fidelity.

Conclusions The VFM is used to successfully determine hyperelastic material properties, and we establish best practice regarding virtual field selection via equalization.

Keywords Magnetic resonance · Virtual fields method · Full field · Material characterization · Elastomer

Introduction

Material characterization leveraging full-field information is presently gaining in popularity, and pioneering work has been done since 1989 by Grédiac, Pierron, Avril, and Hild, among others, on the Virtual Fields Method (VFM). The VFM is based on the principle of virtual work and is used to characterize an object's material properties. By minimizing the difference between the internal and external virtual work, the boundary value problem that combines (1) measured loads and full-field displacements in real experiments and the (2) specified admissible virtual fields is used to solve for unknown material properties [1]. To date, there have been a wide variety of applications of the VFM (discussed in detail in [1]). A sizeable portion of VFM applications has been in characterization of metals and composites in both the linear (including anisotropic and orthotropic samples) [2–6] and non-linear (e.g. elasto-plastic [7]) [8, 9] regimes, while some others have aimed to characterize hyperelastic [10] and bio-materials [11–14] undergoing finite deformations. In the vast majority of these studies, the tests have used single-plane surface measurements, with displacements determined using e.g. digital image correlation [12, 15] or the grid method [16–18]. When images are acquired in 2D, assumptions of plane stress are typically made to approximate the additional components of stress and strain along the third dimension, and characterization then proceeds with the VFM.

However, there is a range of samples or materials in which boundary conditions or geometries or both cannot be straightforwardly designed or chosen to be 2D; the most apparent possibly being bio- and natural materials.

✉ J.B. Estrada
jbestrad@umich.edu

1   Department of Mechanical Engineering, University of Michigan, Ann Arbor, MI, USA

2   Department of Biomedical Engineering, University of Michigan, Ann Arbor, MI, USA

3   Macromolecular Science and Engineering, University of Michigan, Ann Arbor, MI, USA

Mechanical characterization of bio-structural materials, e.g. ligaments and tendons, is particularly difficult. Samples can either be cut and clamped, which results in uncontrollable strain inhomogeneity out of the plane, or left attached to curved bones, which results in non-uniaxial deformation during uniaxial loading [19, 20]. If *in vivo* applications are the end goal, boundary conditions and load direction have practical limitations. As such, without (1) validity of through-thickness deformation assumptions and (2) the ability to control the boundary conditions on our samples, we are left with an unavoidable discrepancy between uniaxial loading and actual deformations in the materials. Thus, we need to acquire fully volumetric deformation fields, moving forward from 2D plus assumptions or 3D-DIC. Fully 3D displacements are more challenging to acquire, usually requiring either some embedded fiducial markers (e.g. fluorescent particles [21] or contrast agents [22]) or enough inherent, roughly isotropic, natural contrast [23] to perform digital volume correlation (DVC) [24] of the material during the deformation process.

For anisotropic, structural tissues, using natural contrast is challenging due to small optical penetration depths with respect to the scales of native tissues, while large, anisotropic repeat-unit structures frustrate the applicability of volume correlation. While some studies have successfully leveraged local contrast for volumetric deformation [25], the translation of optical images of natural, anisotropic materials to mechanical deformation is not always straightforward.

Due to the stated variety of challenges, we turn our attention to an alternate, non-optical method of determining deformation fields in materials: displacement-encoded magnetic resonance imaging (MRI). Displacement encoding MRI experiments yield complex valued 2-D or 3-D maps of an object, in which a voxel's phase (modulo 2π) is proportional to the displacement experienced by protons in that voxel, along a given direction. The measured displacement will have occurred during an interval between an encoding and a decoding segment of a pulsed field gradient (PFG) displacement encoding MRI pulse sequence, in which the interval's duration is typically on the order a second or less. The original displacement encoding sequence is the double-PFG spin echo sequence [26], which was used for the measurement of fluid diffusion coefficients.

Over time a variety of other displacement encoding MRI techniques have come into use toward the shared goal of determining deformations in materials. These largely fall into two classes, the encoding of displacements into the phase of nuclear spins contained within a voxel, or by using MRI sequences to tag an object with a regular pattern then measuring the pattern's deformation as the tagged sample is deformed. As some examples of the former, displacement encoding with spin echoes (DENSE) has been used for the measurement of flow and for the measurement of (cardiac) displacements [27]. Further refinements of DENSE using fast spin echoes (FSE) or balanced gradient sequences (also known as fast imaging with steady state free precession, or FISP) for imaging have been employed by Neu et al. for determining strain in biological materials such as articular cartilage [28] and coupled with finite element analysis [29] and other discrete methods [30] for material property estimation. In the latter category, harmonic phase (HARP) magnetic resonance imaging using tagged sinusoidal gradients have been used to spatially tag material and estimate strain fields, for example as developed for cardiac tissue in 2D [31] and extended to 3D [32], and in other applications such as deformations in the brain undergoing rotational acceleration [33] (reviewed more broadly in [34]).

In this particular study, we utilize a recently developed custom pulse sequence – conceptually related to DENSE – employing a combination of stimulated echoes and spin echoes to encode and read out displacement fields; the sequence was optimized for robustness and efficiency [35]. We present here the image processing pipeline from complex MR data, through finite strain, and finally culminating in characterization of isotropic elastomeric samples using the VFM in full 3D, which we define herein as MR-*u*, in a nod to small-strain magnetic resonance *elastography* (MRE) [36]. We show the pipeline as a flowchart in Fig. 1. Additionally, a kernel-like differentiation filter is derived and presented for complex-valued MR data, analogous to DIC differentiation filters, that divides neighbor pairs of voxels to acquire the local phase gradient without need of implementing unwrapping algorithms. Finally, error analysis relating the technique to the resulting output material properties is pursued and discussed, with recommendations on pulse sequence modifications and data filtration for reducing MR-specific errors and optimizing resulting parameter estimates from the VFM.

MR-*u* Theory

Continuum Mechanics

In this technique, we start by considering an arbitrary solid with volume Ω_0 in its undeformed configuration, as in Fig. 2. The volume Ω_0 has some specified traction and displacement boundary conditions which act on the object's surface $\partial\Omega_0$. The volume Ω_0 is assumed to undergo finite deformation to an experimentally observed state Ω_i, in which an internal point X in the reference state Ω_0 is mapped to a new point x in Ω_i via the displacement gradient tensor on the reference configuration, $\mathbf{F}(X)$,

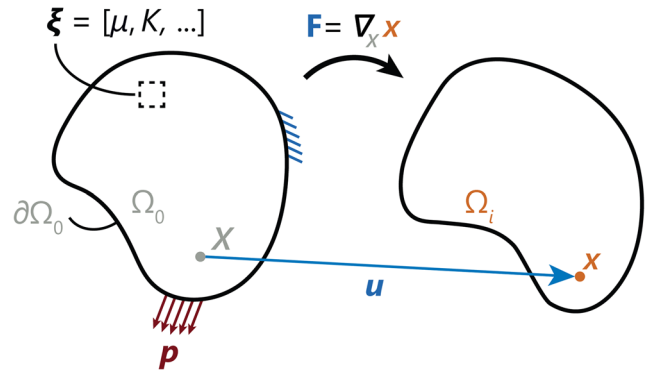$$\mathbf{F}(X) = \nabla_X x = \nabla_X u(X) + \mathbf{I}, \tag{1}$$
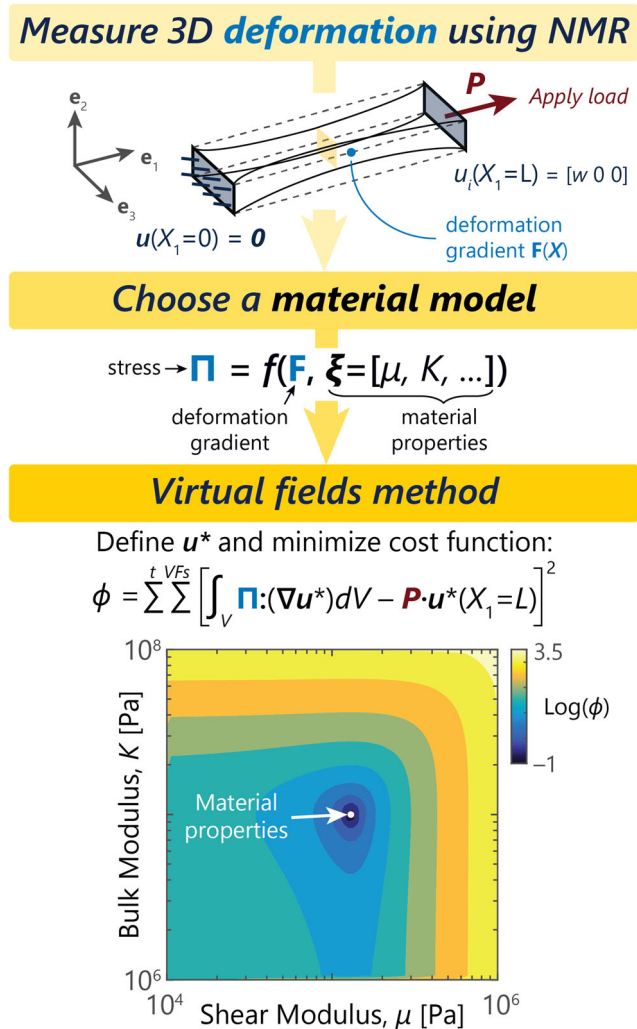
Fig. 1 Flowchart for magnetic resonance characterization. First, a sample is stretched and imaged using nuclear magnetic resonance with the goal of acquiring 3D strain fields mapped to the reference configuration. Then, selection of a suitable material model and virtual fields allows for construction of a cost function ϕ based on the principle of virtual work. This function is minimized in order to find the best estimate for material properties assuming the chosen material model

Fig. 2 Continuum mechanics primer. An object with material properties ξ, initially with volume Ω_0, is subject to applied tractions p and displacement (Dirichlet) boundary conditions at its surface $\partial\Omega_0$, which cause a displacement u of arbitrary point X to x. This deformation is described by the deformation gradient tensor $\mathbf{F}(X)$

In the experimental method presented in this paper, we acquire a phase quantity proportional to the displacement fields $u(X)$, modulo 2π, using nuclear magnetic resonance (NMR), and apply a custom numerical image processing technique to differentiate and determine the entire deformation gradient tensor $\mathbf{F}(X)$ in 3D samples. Furthermore, we measure the force P acting on the stretched sample with a load cell. In general, our goal is to determine the material properties.

Determining Material Parameters via the Virtual Fields Method

Our experimental apparatus measures both the spatially varying deformation fields inside of – and the loads applied to – our 3D material samples. The materials used in this study are silicone rubbers and as such are assumed to be homogeneous, isotropic, and hyperelastic, though the method can be extended to anisotropic hyperelastic materials. The goal is to inversely determine a vector of *a priori* unknown material properties defined within a chosen constitutive model relating the test sample's kinematics to its kinetics. In general, we can write these mechanical properties as a vector, ξ. The strain energy functions and material parameter vectors used in this study are presented in Table 1; in this study we considered functions of the volume-corrected first and second invariants $\bar{I}_1$ and $\bar{I}_2$ of the left Cauchy-Green tensor, $\mathbf{B} = \mathbf{F}\mathbf{F}^\mathsf{T}$ and the Jacobian of the deformation gradient tensor, $J = \det(\mathbf{F})$.

Then to solve for the set of material properties ξ, given our choice of constitutive model, we can harness the VFM, derived from the principle of virtual work. The principle of virtual work is essentially the weak form of the equilibrium equation, and thus, it should hold for any kinematically admissible test function, or "virtual field" $u^*(X)$, that satisfies the experimental boundary conditions. If we have

where the displacement vector, u, of a point is given by the difference in its current and reference positions, $u = x - X$. The object is acted upon in general by tractions $p(X \in \partial\Omega_0)$, but in practice, we measure the total load P acting on a subsurface $S \in \partial\Omega_0$ of the object with a load cell,

$$P = \int_S p(X) dS. \tag{2}$$

The deformations in the object are treated as finite and are assumed to be fully elastic, and as such we can use the Lagrangian strain tensor $\mathbf{E}(X)$ to describe the deformation,

$$\mathbf{E}(X) = \frac{1}{2}\left(\mathbf{F}(X)^\mathsf{T}\mathbf{F}(X) - \mathbf{I}\right). \tag{3}$$

Table 1 Examples of hyperelastic models using a linear bulk term, with their associated material parameters and strain energy density functions

Model	Material parameter vector, $\boldsymbol{\xi}$	Strain energy density function, U
Neo-Hookean	$[\mu, K]$	$\frac{\mu}{2}\left(\bar{I}_1 - 3\right) + K(J - 1)$
Eight-chain [37]	$[\mu, \lambda_m, K]$	$\mu \sum\limits_{i=1}^{5} \frac{a_i}{\lambda_m^{i-1}}(\bar{I}_1^i - 3^i) + K(J - 1)$
Mooney-Rivlin	$[C_{10}, C_{01}, K]$	$C_{10}\left(\bar{I}_1 - 3\right) + C_{01}\left(\bar{I}_2 - 3\right) + K(J - 1)$
Generalized polynomial	$[C_{ij}, K]$	$\sum\limits_{i}\sum\limits_{j} C_{ij}\left(\bar{I}_1 - 3\right)^i \left(\bar{I}_2 - 3\right)^j + K(J - 1)$

properly measured our deformation fields and loads, the equation will be balanced for the correct values for material properties we seek to find.

For both experimental convenience and validation of elastic deformation, our full-field displacement field measurements (and virtual field constructions) are performed as the sample is in its reference configuration, Ω_0. We thus choose to cast the principle of virtual work (assuming a hyperelastic material in finite deformations and static equilibrium) in the following form:

$$-\int_{\Omega_0} \boldsymbol{\Pi} : (\nabla_X \boldsymbol{u}^*)dV + \int_{\partial\Omega_0} (\boldsymbol{\Pi} \cdot \boldsymbol{n}) \cdot \boldsymbol{u}^* dS = 0, \qquad (4)$$

where $\boldsymbol{n}$ is the surface normal to $\partial\Omega_0$. The first Piola-Kirchoff stress is defined as the tensor derivative of the strain energy density function with respect to the deformation gradient tensor, i.e.

$$\boldsymbol{\Pi}(\boldsymbol{\xi}, \mathbf{F}) = \frac{\partial U(\boldsymbol{\xi}, \mathbf{F})}{\partial \mathbf{F}} \qquad (5)$$

In general, it may be easier to perform measurements in either the reference or deformed configuration, which would determine the choice of stress quantity and its virtual strain-like work conjugate that should be used; this is a user preference and need only be consistent [1].

In practice, equation (4) is constructed as a cost function ϕ which is minimized with respect to $\boldsymbol{\xi}$ to determine the best estimate of the material properties, $\boldsymbol{\xi}^*$,

$$\boldsymbol{\xi}^* = \underset{\boldsymbol{\xi}}{\mathrm{argmin}} \left\{ \phi \equiv \sum_{i=1}^{N} \sum_{j=1}^{n_{VF}} \left(-\int_{\Omega_0} \boldsymbol{\Pi}^{(i)} : (\nabla_X \boldsymbol{u}^{*(j)})dV \right. \right.$$
$$\left. \left. + \int_{\partial\Omega_0} (\boldsymbol{\Pi}^{(i)} \cdot \boldsymbol{n}) \cdot \boldsymbol{u}^{*(j)} dS \right)^2 \right\} \qquad (6)$$

where the cost function ϕ is a summation of the square of the internal and external virtual energy mismatch over all virtual fields n_{VF} and all experimental steps N. The minimum value of ϕ that best satisfies the principle of virtual work is henceforth denoted as ϕ^*. Similarly to classical mechanics problems based on the principle of minimum potential energy which aim to choose the correct analytical form for the deformation field before solving for the energy-minimizing field amplitudes, the virtual fields method assumes an analytical form for the constitutive law and

solves for the energy-minimizing material constants. However, the virtual fields in these two cases serve distinctly different purposes; in the former, the virtual deformation field is chosen to be a best guess for the true displacement field, while for the VFM, the virtual fields must adhere to boundary conditions but may be considerably different from the true deformation field. These virtual fields are, importantly, test functions which can either be user-defined [10] or constructed in a procedural or optimized way [38, 39] to best identify material properties. In general, a variety of virtual fields is beneficial for parameter confidence [1], though some considerations of normalizing both (a) the virtual fields n_{VF} with respect to each other and (b) the energy mismatch magnitude to equally weight each deformed configuration N should be taken; both are addressed in the discussion.

Experimental Procedure

Loading Chamber

Briefly, the loading chamber consists of a captive linear actuator (L5918S2008-T10X2-A50; Nanotec Electronic GmbH & Co. KG, Germany) with displacement encoder in series with a load cell (LCM300; Futek Advanced Sensor Technology Inc., Irvine, CA, USA), polyetherimide pull-rod (Ultem, 0.5" OD; McMaster-Carr), and custom sample chamber. During data acquisition the sample chamber is positioned at the center of the 7T MRI apparatus and imaging gradient set (Agilent Technologies, Santa Clara, CA, USA), as shown schematically in Fig. 3. MR signals are excited and acquired with a 300MHz Millipede RF-coil surrounding the sample chamber (not shown). The stepped linear actuator can provide forces of up to 800 N at speeds up to 25 mm/s, with a minimum resolution of 50 µm/step. For the set of experiments reported here, due to low load magnitudes compared to the load cell precision in our setup, the loads at equivalent global deformation states were also measured externally and quasistatically, using an ADMET materials testing system platform (ADMET, Inc., Norwood, MA, USA) equipped with a 25 N load cell. Displacement-controlled input profiles were programmed in Matlab (The Mathworks, Natick, MA, USA) and communicated via
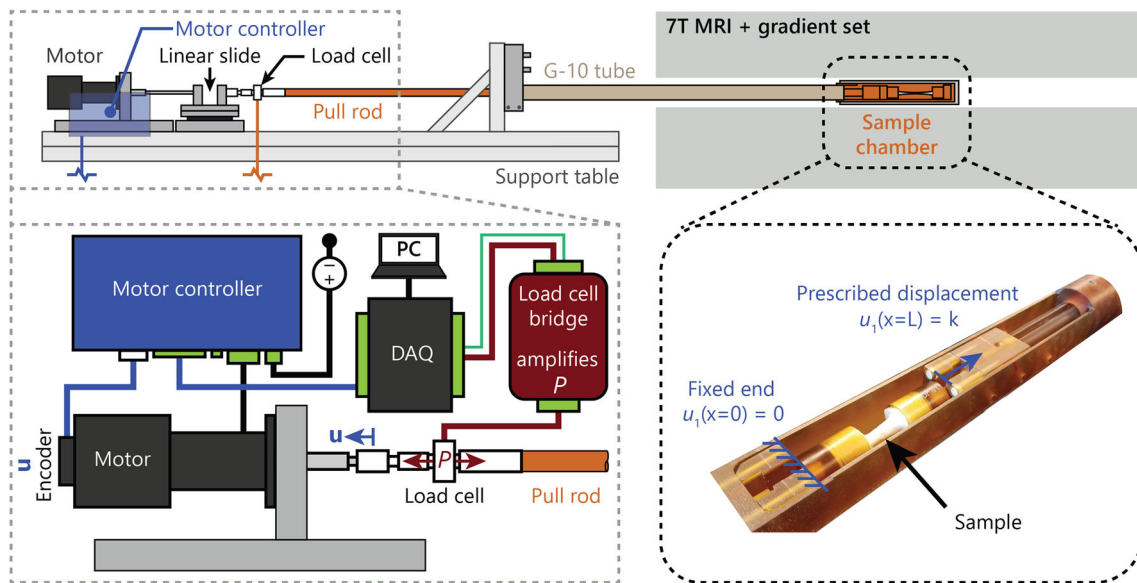
Fig. 3 Experimental setup schematic. A captive linear actuator prescribes a periodic, constant-amplitude, encoder-verified displacement of one edge of a sample, synchronous with a custom NMR pulse sequence which acquires slices of the entire full-field 3D displacement between reference states. Generally, a load cell measures the applied force on the sample, which is balanced by a force-return G-10 tube and custom polyetherimide sample chamber

DAQ to the linear actuator with a motor controller (C5-E-1-09; Nanotec). The custom sample chamber consists of a polyetherimide (Ultem, 1.5" OD; McMaster-Carr) outer housing that mounts directly to a glass-fiber-reinforced epoxy tube (G-10 grade, 1-1/8" OD; McMaster-Carr). The opposite end of the G-10 tube is rigidly clamped to the aluminum T-slotted 80-20 structural frame, such that force return for the induced load during displacement is carried through the G-10 tube and symmetrically balanced by the frame. During testing, one side of the sample is rigidly gripped at the far chamber edge, while the other side is gripped on the side controlled by the actuator. Axial force is carried via the rigid polyetherimide pull-rod, which is ensured to be torsion-free by addition in series of a custom frame-mounted linear slide with thrust bearings. The pull-rod is kept aligned during motion by custom uniaxial polytetrafluoroethylene (PTFE, 1" OD; McMaster) bearings in the G-10 tube. During testing, stretching of the sample and the MR pulse sequence are synchronized using TTL pulses.

Sample Fabrication

Silicone samples (Dragon Skin; Smooth-On Inc., Macungie, PA, USA) were created by manually stirring two liquid precursors, slowly degassing the mixture in a vacuum chamber, carefully pouring it into custom laser-cut Delrin molds, and curing it at room temperature. The silicone samples were affixed to laser-cut Delrin platens via quick-drying adhesive (Loctite Plastics Bonder; Henkel, Milano, Italy) which were in turn glued to 1/4-20 nylon socket head

cap screws (McMaster-Carr, Atlanta, GA, USA), and placed in the loading chamber. Standard 3D gradient echo images of the sample were acquired at high resolution (0.2 mm), to verify sample positioning in the MRI apparatus and to aid in masking during image processing.

Magnetic Resonance

Traditional digital image or volume correlation yields displacement fields by *a posteriori* correlation of image contrast patterns, via computerized image processing: one extracts displacement fields relating the contrast pattern of a stretched state to that of a reference state, essentially comparing a stretched map of features with the un-stretched reference map (Fig. 4a). By contrast, with displacement encoding MRI, which like all MRI imaging yields complex valued image data, one produces one 3D-MRI image of a sample's reference state in which the difference of displacements associated with the two sample conformations, stretched and reference, is encoded directly into the phase of the complex reference image (Fig. 4b). We employ the APGSTEi [35] imaging sequence to accomplish this. The sequence is an imaging variant of the non-imaging APG-STE sequence described in [40], assembling a full 3D image from a stack of contiguously acquired 2D slices. The sought-after information is found in the phase of each voxel which, modulo 2π, is proportional to the distance that protons in a voxel have moved as the sample was taken from the stretched configuration, where position is encoded, to the reference configuration where position is decoded.
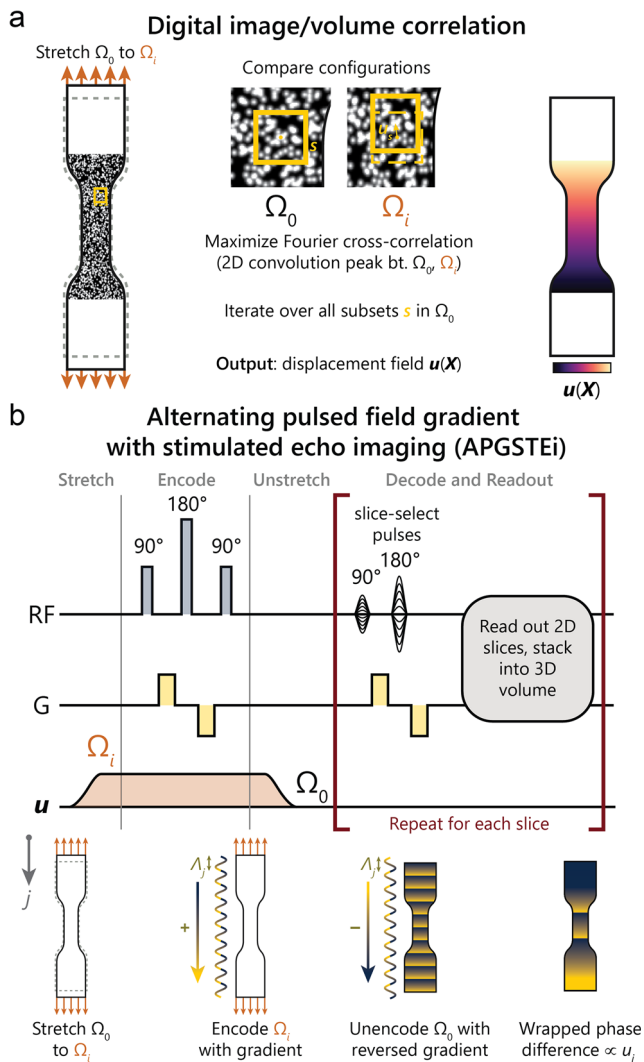
Fig. 4 Comparison of digital correlation and APGSTEi. (**a**) In digital image/volume correlation, two deformation states are imaged and compared to get local displacement, commonly by maximizing a cross-correlation function of subsets in Fourier space. (**b**) APGSTEi produces one complex-valued (3D) image of the reference configuration in which the displacements connecting the sample's deformed configuration to the reference configuration are directly encoded in the phase of the image; each displacement component corresponds to one applied gradient direction and acquisition. Displacement encoding is performed using encoding and decoding pulsed field gradients shown in yellow

This phase encode of displacements – the difference of proton positions in the stretched and reference states – is accomplished with equal amplitude opposite polarity pairs of position encoding and decoding of gradient pulses, shown in yellow on the gradient (G-)line of Fig. 4.

The phase difference between reference and deformed configurations is locally proportional to our displacement field $\boldsymbol{u}$ modulo 2π,

$$\boldsymbol{\theta}(X) = \gamma_H t_e \boldsymbol{G} \boldsymbol{u}(X) = \frac{\boldsymbol{u}(X)}{\Lambda}, \qquad (7)$$

where the vector field $\boldsymbol{\theta}$ is the angle of the complex vector field output from the MR, $\boldsymbol{Z}$, given by

$$\boldsymbol{\theta}(X) = \text{angle}(\boldsymbol{Z}(X)) = \arctan\left[\frac{\text{Im}(\boldsymbol{Z}(X))}{\text{Re}(\boldsymbol{Z}(X))}\right], \qquad (8)$$

and γ_H is the gyromagnetic ratio, t_e is the effective encoding duration of the pairs of encoding and decoding gradient pulses, $\boldsymbol{G}$ is the respective magnetic field gradient, and the product Λ combines these parameters together in terms of a user-adjustable phase-encoding wavelength in the three orthogonal Cartesian directions. Procedurally, displacement encoding pulsed field gradients are applied in separate experiments for each corresponding phase field component. Thus, each full data set is comprised of three acquisitions, one for each Cartesian direction.

Loading and Imaging Procedure

Samples were stretched, encoded with pulsed field gradients in the deformed configuration, and unencoded after unloading to the reference configuration following the pulse sequence (described in greater detail in [35]) and calibration procedure described in the appendix. The resulting phase information stored in the complex MR reconstruction represents the wrapped vector components of the change in position, or displacement. As the range of the arctan function, and thus our phase angles, is restricted, the displacement field if not unwrapped contains sharp, discontinuous boundaries which produce significant spurious strain peaks. The user may ameliorate these false peaks via two methods: adjusting Λ_k and choosing an numerical differentiation scheme.

First, while the encoding length Λ_k can be chosen by the user, an overly short Λ_k, given thermal and systematic error effects, can introduce or accentuate these phase unwrapping artifacts. Some consideration of choice of Λ_k should therefore be taken for minimizing phase unwrapping artifacts; a good rule of thumb is to set the encoding length to approximately twice the voxel size, and increase it if the phase wraps appear unclear during larger prescribed displacements. In this study, the encoding length Λ_k in each direction was chosen to be 1 mm, sufficiently long to minimize phase gradient error for all load steps. Voxel sizes were chosen to be $0.43 \times 0.5 \times 0.5$mm, corresponding to $128 \times 32 \times 32$ voxel images.

Second, treatment of phase wrapping artifacts is an active research area, with recent 3D unwrapping algorithms employing different methods for determining phase reliability [41], treatment of noise [42], and other potential continuity pitfalls. While advances in three-dimensional phase unwrapping continue to be made, in this study we

instead employ a useful numerical phase gradient operation using complex division described in the following section, inspired by convolution-based image differentiation techniques to directly determine phase (and therefore displacement) gradients.

## Numerical differentiation for strain calculation

Numerical differentiation for strain calculation in full-field and/or image-based techniques typically uses one of two methods – an analytical fit to or mesh construction for the displacement field and subsequent direct differentiation of displacement to get strain, or a numerical approach in which a differentiation operator filter is passed over (convolved with) the displacement field [43]. We choose to follow the convolution-like numerical approach, but in a necessarily modified way for our complex magnetic resonance output (Fig. 5).

Rather than unwrap and subsequently differentiate the phase field θ, a combined complex division operation on the complex MR output Z was utilized to the same effect, as shown in Fig. 5(d). This complex division + differentiation operation is somewhat akin to convolution; from here on we refer to it as *divolution*, and we describe it in more detail in Appendix A.

Rigid motion calibration of the MR

MRI imaging and displacement-encoding are accomplished via pulsed field gradients produced by the imaging gradient set of the MRI apparatus. The set is comprised of three gradient coils – one for each Cartesian direction – which are designed by the manufacturer to produce approximately uniform pulsed field gradients when energized with a current pulse. Deviations form uniformity in the gradient field lead to spatial distortions of the reconstructed image, and to systematic errors in the phase maps produced by displacements. Similar distortions and errors have been identified and corrected in earlier, related work on phase contrast MRI employed for velocity imaging [44].

We need to correct for systematic errors in measurements of geometry and displacements for fidelity of $\mathbf{F}(X)$, and in turn, our material properties ξ^*. Material volumes undergoing large displacements acquire both the desired phase shifts that are due to encoding and unencoding at different positions, as well as an additional small error phase shift due to the very slight non-uniformity of the gradient strength within the MRI-active region of the MR imaging machine. The error phase associated with non-uniform gradients translates into false displacement and strain signatures, which are functions of displacement amplitude and the position of the sample
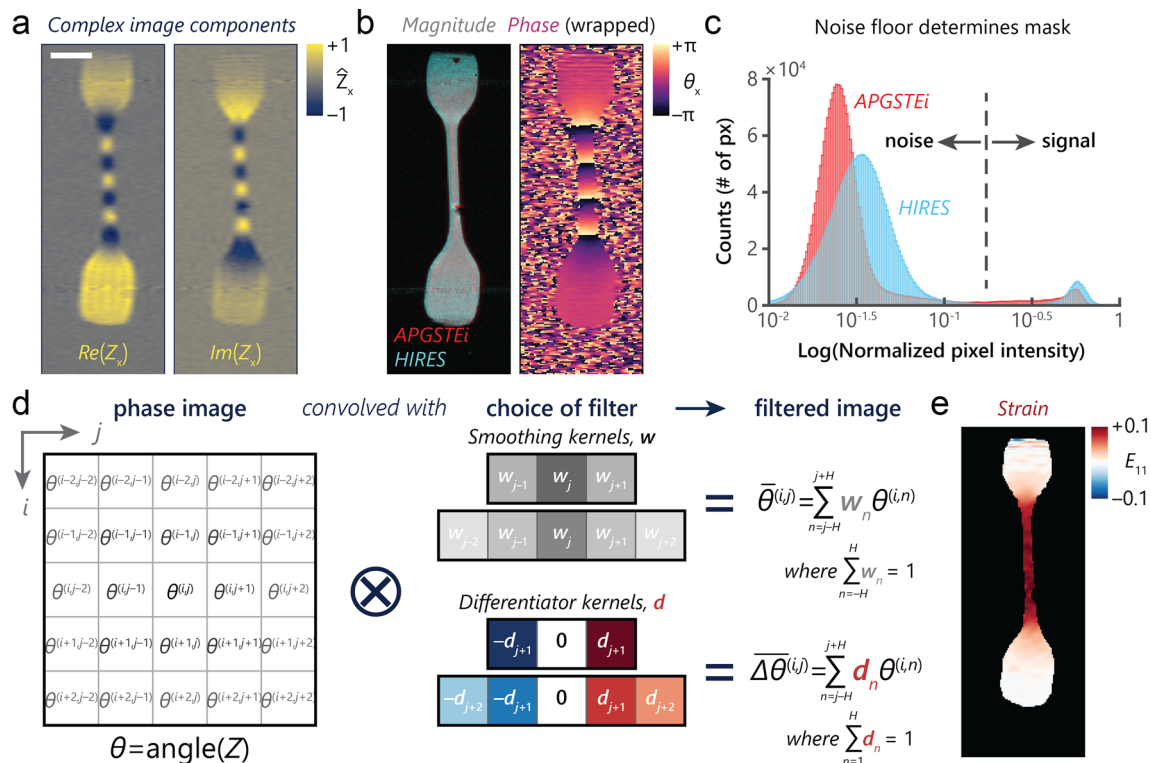
Fig. 5 Processing pipeline from complex MR output to 3D strain tensor field. (**a**) The complex MR vector field output, Z, is acquired for each Cartesian direction. Scale bar 5 mm. (**b**) The magnitude and phase of Z represent magnetic signal and, from our pulse sequence, displacement, respectively. (**c**) A mask is created from the magnitude of Z while (**d**) the phase image is numerically differentiated in complex space by a convolution-like operation. (**e**) Lagrangian strains are composed from the displacement gradients

within the MRI apparatus. Both of these quantities are known, and the systematic error phase can be calibrated out as described below, using the known position of the sample and data acquired in separate calibration data. As a first-order approximation, we can divide the spatial systematic error contributions into (1) a real-space dilation, essentially due to a scalar calibration factor relating the nominal gradient strength to a 'true mean gradient' strength, and (2) a phase accumulation due to gradient non-uniformity. To correct for these two specific error sources, two calibration samples were tested.

The effect of spatial dilation was characterized as a function of sample position in the magnet using an additively manufactured, vertically stacked set of four polymer trays (resembling miniature ice-trays) and containing 32 cubic wells each, in a regular 4×8 array. Each individual well was sized 3×3×3 mm, with 2 mm spacing between adjacent wells. Silicone was cast into these wells and subsequently degassed, and trays were stacked vertically on top of each other to form a 3D MR calibration grid sample comprised of equal sized and equidistant silicone cubes on a Cartesian grid. The regular geometry permitted the quantification of local warping effects in our spatial reconstruction.

A second calibration experiment allowed us to quantify the spatial variation of applied pulsed field gradients. To probe this we first manufactured a rectangular prism sample by pouring silicone into an additively manufactured rectangular box with inner well dimensions 38 mm×18 mm× 17.5 mm. The silicone-filled box was placed into the sample chamber shown in Fig. 3 but attached only to the moving sled for rigid translation experiments. For calibration the sample was translated by controlled amounts. Full phase fields $\theta(X, w)$ were acquired for two different rigid translation amplitudes w inside the large silicone sample, and processed via the procedure defined in Fig. 5. We found that the measured displacement gradient fields, owing purely to slight gradient coil non-linearity, were both increasingly non-zero toward the periphery of the coil and directly proportional to the displacement amplitude (discussed in more detail in Appendix B). Higher-order corrections were then determined functionally via polynomial surface fits, taking into account winding symmetry of the coil for inclusion of odd or even terms, and applied directly as a correction to all measured deformation gradient fields.

Results and Discussion

Deformation Fields

Four samples were tested; the details of each sample are listed in Table 2. Three stiffness grades of silicone were used, with company-specified nominal durometer ratings of 2A, 10A, and 20A. Samples were prepared according to manufacturer recommendations at the standard 1:1 two-component mixture ratio in all cases prior to degassing and casting. Two distinct geometries were used: a rectangular prism of approximately $40 \times 8 \times 7.5$ mm^3 (henceforth called "I-block"), and a slightly S-shaped geometry of constant cross-section ("S-block see"; [35]) of similar dimensions. Each of these samples was glued with cyanoacrylate to platens and stretched longitudinally, as schematically depicted in Fig. 6. Deformation fields are acquired with the procedure described in Fig. 5, at a resolution of $\chi_{\mathrm{res}} = [0.4375, 0.5, 0.5]$ mm. Thus, with a sample of approximate dimensions $40 \times 8 \times 7.5$ mm, there are approximately 22,000 volumetric data points per load level, each containing the full deformation gradient tensor $\mathbf{F}(X)$. This resolution has an associated temporal cost of approximately 12 minutes per displacement component (as the material is cycled once every 3 s), for a total of approximately 45 minutes per load level. The normal and shear components of the full strain tensor for sample '10A I-block 1' stretched to 4.5 mm are shown in Fig. 6(b) and (c), respectively. As expected, the majority of the I-block exhibits a uniaxial deformation state, while in-plane shear dominates near the glued edges of the sample. Furthermore, the E_{23} component corresponding to twist in the sample is low, suggesting good sample alignment during loading.

Virtual Fields

Selection of virtual fields

As discussed in Section "Determining Material Parameters via the Virtual Fields Method", the VFM harnesses the principle of virtual work, or the weak form of the balance of linear momentum, to inversely determine material

Table 2 Experimental sample details for silicone experiments

Sample #	Material	Approximate dimensions ($l \times w \times h$), [mm]	Name	# Load levels
1	2A-grade silicone	rectangular prism ($39 \times 8 \times 7.5$)	2A I-block	$N = 5$
2	10A-grade silicone	rectangular prism ($41.5 \times 8 \times 7.5$)	10A I-block 1	$N = 9$
3	10A-grade silicone	rectangular prism ($39 \times 8 \times 7.5$)	10A I-block 2	$N = 3$
4	20A-grade silicone	'S'-shaped prism ($39.5 \times 8 \times 6.5$)	20A S-block	$N = 6$

Fig. 6 Representative 3D deformation field for a stretched I-block. (**a**) Silicone I-blocks (straight, rectangular prisms) are glued to platens, stretched via an applied load P, and imaged, resulting in 3D strain fields. (**b**) Normal strains exhibit expected uniaxial-type behavior of longitudinal extension and equal transverse contraction, while (**c**) shear strains concentrate at edges in the case of E_{12} and E_{13} and are small for the twist E_{23} component. (**d**) Admissible user-defined virtual fields can then be chosen in accordance with the strain boundary conditions
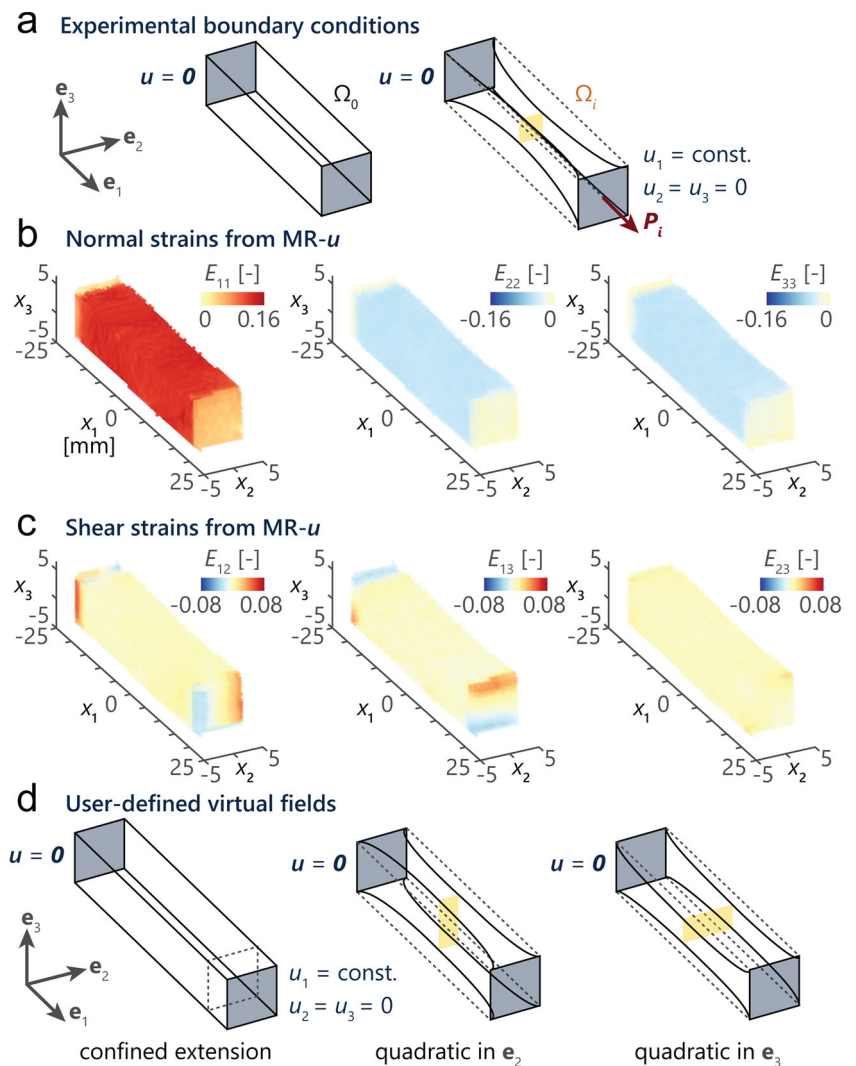
properties via minimization of a virtual-energy-mismatch-based cost function, ϕ, where

$$\phi \equiv \sum_{i=1}^{N}\sum_{j=1}^{n_{VF}}\left(\int_{\Omega_0}\mathbf{\Pi}^{(i)}:(\nabla_X\mathbf{u}^{*(j)})dV\right.$$
$$\left. - P\cdot u_1^{*(j)}(X_1=L)\right)^2. \quad (9)$$

In the internal virtual work (first) term, the first Piola-Kirchoff stress $\mathbf{\Pi}(X) = f(\mathbf{F}(X), \boldsymbol{\xi})$ is a function of the MR-derived deformation gradient tensor and material properties for a chosen material model, $\mathbf{u}^{*(j)}(X)$ is the j-th selected virtual field. The external virtual work (second) term is defined by the product of the actual load applied to the sample, P, and the virtual displacement at the moving end of the sample. Thus, the experimentally measured full-field data plus guesses for constitutive parameters replace the stress term of the cost function, while the quantities with which they are contracted are the test functions, or

virtual fields, that must only obey the boundary conditions of the problem. While any non-trivial admissible field satisfies minimization of the cost function for the true material parameters, virtual fields that probe the material's response to various kinds of deformation, such as those seen in Fig. 6(d), provide best parameter confidence. Another option, provided the data are sufficiently trustworthy, is to use the measured deformation field directly as the, or a, virtual field. Both cases – using (a) the three simple analytical fields and (b) the experimentally measured deformation field – were considered in this study as potential options and compared.

Equalizing virtual fields and weighting cost function

The cost function ϕ is a double summation, ranging on (a) the total number of virtual fields included in analysis, n_{VF}, and (b) the number of included global load levels N. A potential side effect of summing over N and n_{VF} is that individual noisy terms, or terms scaled poorly to one

another, may dominate the cost function landscape. As such, we correct for the relative energy scaling disparity for these two summations by the following method. First, we correct, or equalize, the approximate magnitudes of the l^2-norms of the virtual field gradients,

$$\nabla \hat{u}^{*(j)} = \frac{\nabla u^{*(j)}}{\text{mean}\left(\|\nabla u^{*(j)}(X)\|\right)},$$

$$\text{where mean}\left(\|\nabla u^{*(j)}(X)\|\right)$$

$$= \frac{1}{V_{\Omega_0}} \sum_{dV_{\Omega_0}} \|\nabla u^{*(j)}(X)\|. \qquad (10)$$

The effect of virtual field equalization can be pronounced on cost function space, as described in detail in the following section with a simulation of a rectangular prism "I-block", as shown in Fig. 7(a) and (b). In this figure, Fig. 7(a) shows the cost function space for the set of user-defined fields ∇u^* from Fig. 6(d)s constructed with a 10% maximum displacement gradient in the volume Ω_0. In the cost function contours of Fig. 7(b), the virtual fields $\nabla \hat{u}^*$ have been equalized. While the VFM-determined material properties converge in both cases to the input simulation values of $[\mu, K] = [130 \text{ kPa}, 10 \text{ MPa}]$, the cost function space changes drastically, with the global minimum definition improving markedly.

Furthermore, some parameters may be active in different regimes of stretch, for example a small-strain response versus large-strain locking stretch-type behavior. To ameliorate this effect, we can correct the cost function by an energy quantity that we can choose to either equally weight all data points or scale with increasing energy values. In practice, a useful quantity is the actual external work applied to the sample, which can be found as the dot product of the applied load and edge displacement (assuming one side fixed as in our experiments). We then choose either to normalize our cost function by (a) the external work done at the sample's respective step or (b) the maximum external work done on the sample during an entire experiment. The normalized cost function can be written as

$$\hat{\phi} = \sum_{i=1}^{N} \sum_{j=1}^{n_{VF}} \left(\frac{\int_{\Omega_0} \Pi^{(i)} : (\nabla_X \hat{u}^{*(j)}) dV - P \cdot \hat{u}_1^{*(j)}(X_1 = L)}{EW} \right)^2,$$

$$(11)$$

where the external work EW can be defined as either $\max(EW) = \max[Pu_1(X_1 = L)]$ or $EW_i = [Pu_1(X_1 = L)]_i$. Figure 7(c) highlights the improvement on convergence to the minimum value for the second order term due to a higher relative weight on larger strain data. While both data normalization cases converged to global minima at the prescribed ξ, the relative energy mismatch is much higher for the dominating large values of stretch.

The choice of equalization and normalization is best left to the user, but all cases were considered in general and are discussed further in Section "Effects of near-incompressibility of experimental samples".

Material Property Identification and Challenges

To identify the best estimate of material properties, we must minimize the (if desired, normalized) cost function, $\hat{\phi}^* = \min\left(\hat{\phi}\right)$ of equation (11). The minimization procedure was performed with a reflective-boundary modification of the simplex, or Nelder-Mead algorithm [45], which was found to converge well for these cost function spaces, but in general, the minimization algorithm may be chosen by the user. As a baseline metric, we compare least-squares error values within a certain threshold from the minimum to estimate the deleterious effect of noise and subsequent potential benefit of data filtering. Other error quantification methods exist for VFM with DIC (e.g. the coefficients of variation approach in [1]), but we choose to look directly at the cost function space, in a manner similar to the sensitivity study performed by Pierron et al. [5], as this method illustrates the information of interest.
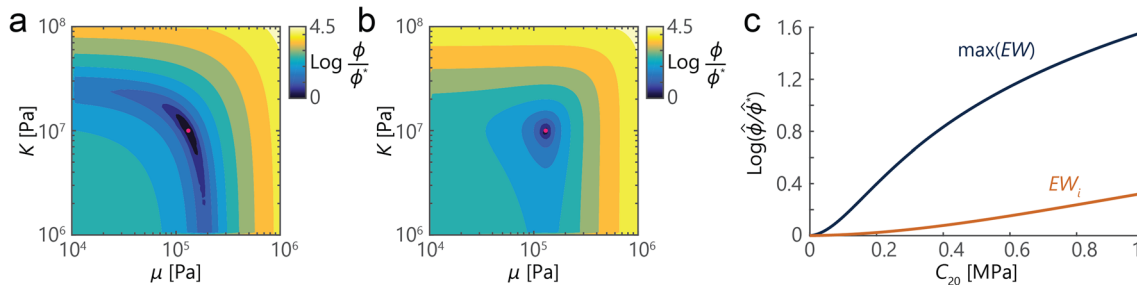
Fig. 7 Comparison of ϕ-space for virtual fields with and without equalization. (**a**) Least-squares error (ϕ-)space can be dominated by choices of individual virtual fields without a suitable normalization scheme, which can manifest in complex topology. (**b**) By equalizing chosen virtual fields procedurally, ϕ-space definition improves. (**c**) Higher order term confidence is additionally affected by the data normalization procedure, in which the cost function can be corrected either proportionally to the global energy state per step, or the maximum global energy state

Noise and filtering effects

In Section "Rigid motion calibration of the MR" we corrected for residual non-uniformity of the gradient fields produced by the MRI equipment, a systematic correction for distortions and errors attributable to the non-ideal nature of the MRI apparatus; it is the same for all our experiments. We next turn our attention to two other sources of error which may be different from one experiment to the next, thermal noise and small amplitude and phase oscillations in the complex MRI image; the latter are essentially due to noise spikes occurring during the MRI data acquisitions. To investigate the expected effects of untreated noise, as well as the effect of data filtering on both clean and noisy datasets, we constructed two simulation cases using approximately the same mesh resolution as our raw data volumes from the MRI. Two distinct cases were considered – the "I-block" geometry (Fig. 8, right column), consisting of a rectangular prism of dimensions $40 \times 7 \times 3$ mm and a "Z-block" geometry (Fig. 8, left column), with length 40 mm and edge cross-section 8×6 mm, and a 12 mm central segment of cross-section 12×6 mm (see insets, Fig. 8(a)). Both cases were taken as Neo-Hookean with shear modulus $\mu = 130$ kPa and bulk modulus $K = 10$ MPa (shown as a green circle on the cost-function space), and meshed at 0.5 mm isotropic voxel size. Only the small $X_2 - X_3$ faces were fixed in all displacement components, and the face corresponding to the experimental moving sled was displaced to five different distances, $w = 0.5, 1, 2, 3, 4.5$ mm. For cases without filtering or noise (Fig. 8(a)), the deformation gradient tensor $\mathbf{F}(X)$, the load P, and the displacement step were then put through the post-processing virtual fields method pipeline for material characterization.

Addition of synthetic Gaussian and sinusoidal noise (Fig. 8(b)), respectively, was achieved by direct addition to the components of the deformation gradient tensor,

$$\widetilde{F}_{ij}^{\text{gauss}}(X) = F_{ij}(X) + 0.02N(X),$$

$$\widetilde{F}_{ij}^{\text{sine}}(X) = F_{ij}(X) + 0.02\sin\left(\frac{2\pi X_1}{\chi_1^{\text{res}}} + \frac{\pi}{4}\right), \qquad (12)$$

where $N(X)$ is a random, spatially varying normal distribution and χ_1^{res} is the pixel resolution in the longitudinal direction. Pristine and noisy simulation cases were then treated with a k-space Gaussian filter, corresponding to an isotropic real-space kernel size of 0, 1, 2, 4, or 8 voxels. As a metric to compare the relative confidence in the minimum least-squares estimate for material parameters, $\boldsymbol{\xi} = [\mu, K]$, based on the applied load and deformation gradient tensor put through the VFM with the three analytical user-defined fields, we plot contours of a 0.5 dB threshold from the minimum value of $\hat{\phi}$ (contours, Fig. 8 all panels). In the case of pristine data (Fig. 8(a)), adding a blurring
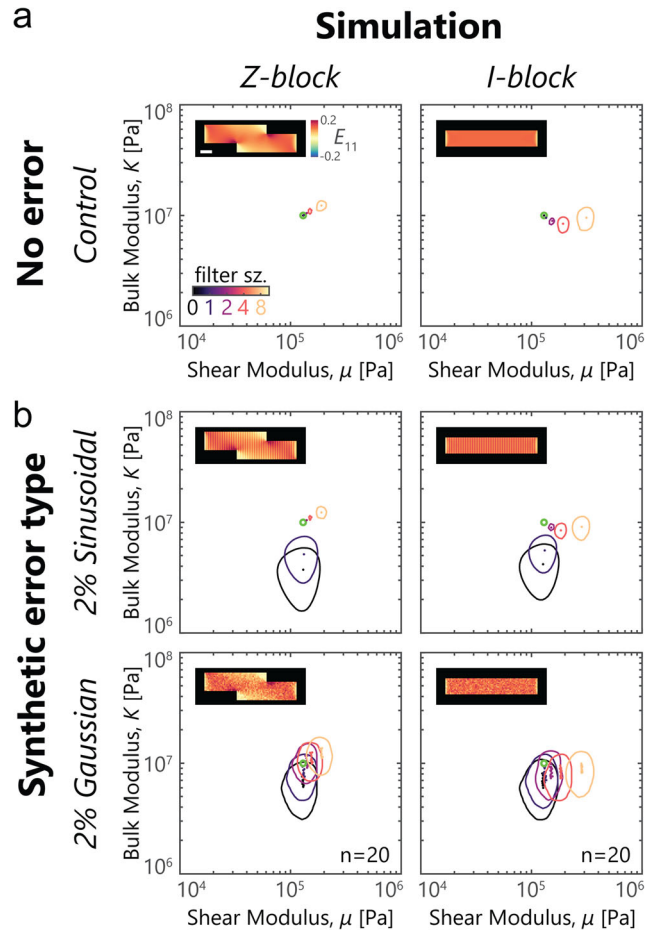
Fig. 8 Modulus estimates as a function of filter size and noise type. (**a**) In the case of two finite element simulation end-to-end stretch cases without noise (longitudinal normal strain field inset, scale 5mm), shear and bulk modulus estimates are increased by applying Gaussian filters of increasing size. The prescribed Neo-Hookean parameters of $[\mu, K]$ = [130 kPa, 10 MPa] are denoted by the green circles. Contours are constant ratios of $\log(\hat{\phi}/\hat{\phi}^*) = 0.5$ and their sizes signify relative flatness of the space. (**b**) In the case of spatially sinusoidal fluctuations and randomly-distributed Gaussian error on the components of the deformation gradient tensor, modest filtering has a benefit on both $\hat{\phi}$-space and best fits

filter generally increases the apparent stiffness of the material, which is attributable to reduction of high-frequency, large strain values near boundaries. Loads are unaffected by filters on the deformation gradient, so the internal virtual work term in turn converges to stiffer mechanical properties to balance the blurring-agnostic external virtual work term. Similarly, the confidence in material parameters, roughly inversely proportional to the size of the contour, correspondingly decreases as we increase our filter size. Upon adding untreated sinusoidal noise to the two simulation data cases (Fig. 8b, top row), the material property estimates become considerably less precise and less accurate, particularly in the estimate of the bulk modulus. As we increase the filter size to above the frequency of the sinusoid (specifically,

twice the pixel size, or $2\chi_1^{\text{res}}$), the systematic error is treated and material property estimates converge to the no error case. In contrast, Gaussian noise impacts precision more variably, due largely to the range of possible energy contribution from the noise itself. Twenty distinct Gaussian noise distributions were tested. Notably, the accuracy in the shear modulus without filtering and apparent stiffening with smoothing filter size generally follows the same trend as the sinusoidal and no-noise cases. However, the bulk modulus estimate, just as in the sinusoidal error case, became both considerably less precise and less accurate than the shear estimate upon Gaussian noise addition. This can be attributed to (1) noise scaling with the cubic product of stretches for J (and hence K) vs. the quadratic scaling of $\bar{I}_1$ (relevant to finding μ) and (2) the larger relative noise contribution to the magnitudes of $J(X)$ compared to $\bar{I}_1(X)$, as shear strains in the prescribed deformation states far exceeded volumetric strains. In general, we conclude that light filtering is acceptable for perhaps very noise-sensitive parameters, but not necessary or even beneficial in all cases.

Effects of near-incompressibility of experimental samples

While silicone is a suitable material for characterization using MRI due to its intrinsic T_1 signal, it is also known to be near-incompressible; methods for characterization of rubber frequently use the assumption of incompressibility and assume a large bulk modulus, e.g. 10^5 MPa [46]. To verify that this is a suitable assumption, we can manipulate the deformation gradient tensor $\mathbf{F}(X)$ to get the principal stretches and the volumetric expansion. We start by decomposing the gradient set- and baseline-corrected $\mathbf{F}(X)$ uniquely into rotation and stretch operations via the right polar decomposition, and proceed to get the eigenvalues of the stretch portion of $\mathbf{F}$, which are three principal stretches $\lambda_i(X)$. While the sample is not exactly in uniaxial tension, particularly near the grips, the middle, unbounded portion can be approximated as uniaxial tension to serve as a useful analytical comparison.

Figure 9 shows a composite of full-field data, specifically, violin plots of stretch values at >13,000 non-edge points in the middle 50% of an I-block sample, $\bar{A}_0$, in the more conventional stress-stretch form. In Fig. 9(a), the average nominal stress, determined from the applied load divided by the average MRI-determined cross-section over the sample mid-section, is plotted against the longitudinal stretch. Each longitudinal stretch group represents the histogram distribution of the longitudinal stretch over all points in the included mid-section. Figure 9(b) similarly shows the average nominal stress plotted against the distributions of transverse stretches $\lambda_2(X)$ (red) and $\lambda_3(X)$ (blue). Finally, Fig. 9(c) depicts the hydrostatic pressure vs. volumetric strain; the hydrostatic component of the average Cauchy stress, $\frac{1}{3}\text{tr}(\boldsymbol{\sigma})$, is plotted against the distributions of the volume change, defined as the determinant of the deformation gradient tensor, $J(X) = \det(\mathbf{F}(X)) = \lambda_1(X)\lambda_2(X)\lambda_3(X)$, minus unity.

As expected for silicone, the values for $(J - 1)$ center nearly exactly around zero, with a mean value of included points in the final stretch state of 4.03×10^{-5}. However, while the distributions of $(J - 1)$ are centered closely around zero, the slight asymmetry in the tails leads to noisy, non-zero energetic contributions via the bulk modulus term in the cost function. The result, in practice, is an inability of the solver to converge meaningfully to an estimated value for the bulk modulus, commonly by simply reducing the bulk modulus estimate to nonphysically low values or zero. Given the noise floor of approximately 0.5% on J from Fig. 9(c), it's practical to instead assume incompressibility and that deviation of $J(X)$ from unity is due to measurement noise rather than actual bulk deformation.

The experimentally-measured stress-stretch curves are overlaid with the predicted uniaxial response with the virtual fields method best-fit shear modulus of $\mu = 27.8$ kPa from the one-parameter Neo-Hookean material description in Fig. 9(a–c). Notably, there is excellent agreement of the uniaxial tension prediction and the stress-stretch plots for both longitudinal and transverse stretch values, suggesting validity of the incompressible assumption. The slight difference between the transverse stretches λ_2 and λ_3 (the mean difference of transverse stretches for all points and load steps is 4.77×10^{-3}), which are expected to be equal in uniaxial tension, can be attributed to a combination of (a) slight shear during loading of the sample, potentially due to slight sample misalignment during loading and (b) noise arising from numerical gradient operations, which may be different in the 2D acquisition plane compared to in the slice-wise acquisition direction.

Silicone Property Estimates

Table 3 highlights the best material property estimates, $\boldsymbol{\xi}^*$, for incompressible first- and second-order first invariant-based models using the VFM on four sets of deformation fields acquired with APGSTEi and separately measured loads. A pair of aforementioned data processing options are compared, specifically the choice of virtual fields (a selection of three user-defined fields versus using the measured deformation field as the virtual field) and choice of data equalization scheme (normalizing the cost function by each individual energy state or a maximal energy state). Strain energy potentials were assumed to behave incompressibly by removing the bulk-dependent term; essentially we assume that since the loads on the material are relatively small and the expected bulk modulus is very

Fig. 9 Comparison of '10A I-block 1' midsection experimental data to uniaxial tension predictions. Violin plots of nominal stress values (applied load versus mean cross-sectional area from MRI) versus (**a**) distributions of longitudinal stretch and (**b**) transverse stretches. Dashed line represents incompressible uniaxial solution using VFM result ($\mu = 27.8$ kPa) assuming the deformation field as the virtual field and equal data weighting. (**c**) Hydrostatic Cauchy stress versus volume expansion ($J - 1$) highlights the apparent incompressibility of the sample and challenge in bulk modulus estimation. In all cases inner boxplots are interquartile and the mean is shown in orange
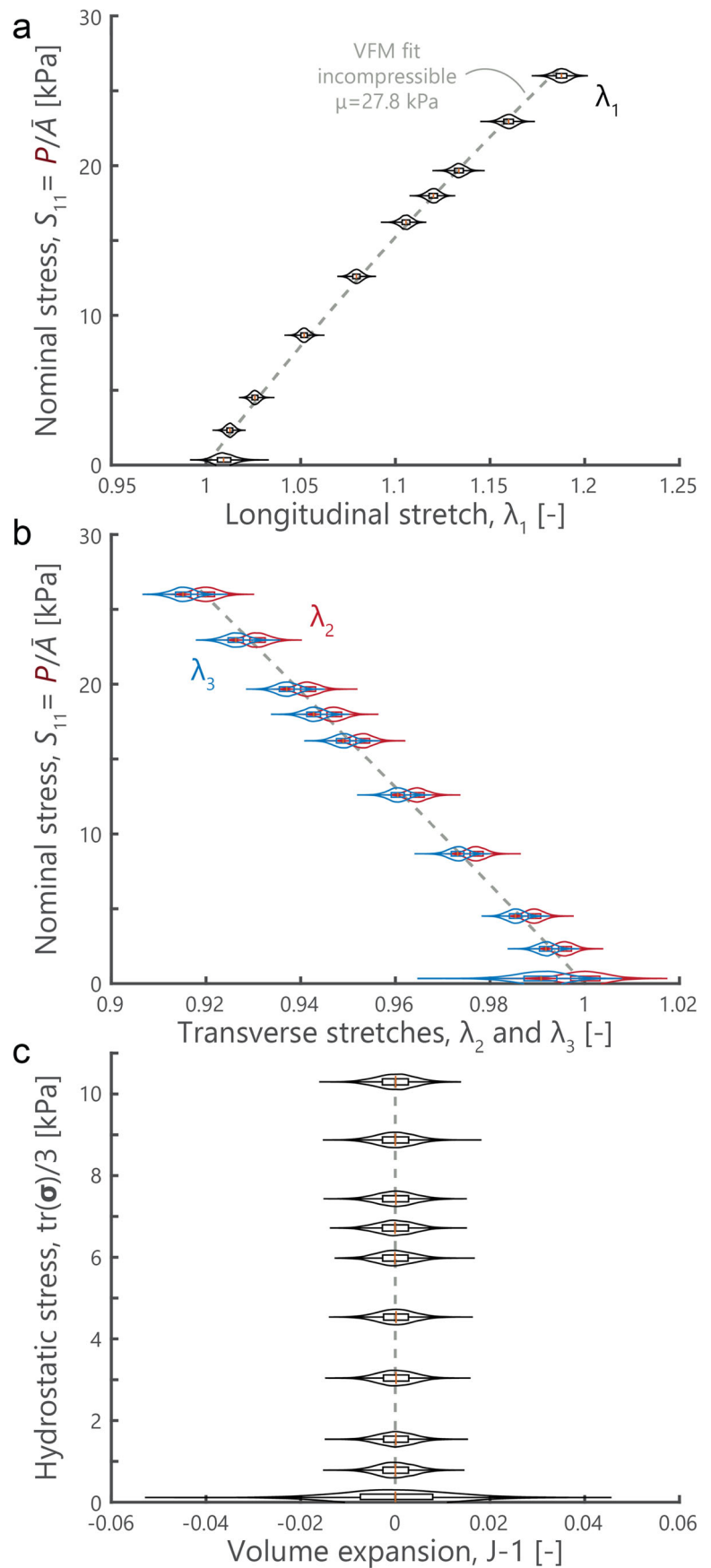
Table 3 Experimental material parameter best estimates $\boldsymbol{\xi}^*$ for first and second order $\bar{I}_1$ material models using MR-$\boldsymbol{u}$

Virtual field choice	User-defined virtual fields		Using $\boldsymbol{u}(X)$ as $\boldsymbol{u}^*(X)$		Uniaxial curve-fit
Data equalization	$EW^{(i)}$	$\max(EW)$	$EW^{(i)}$	$\max(EW)$	
Neo-Hookean C_{10} [kPa]					
2A I-block ($N = 5$)	19.7	17.9	19.2	18.1	19.5±0.6
10A I-block 1 ($N = 9$)	28.3	24.6	27.8	26.0	27.7±0.4
10A I-block 2 ($N = 3$)	32.5	30.5	31.4	29.8	30.6±5.6
20A S-block ($N = 6$)	133.4	116.9	133.3	121.5	
Second order polynomial					
C_{20} [Pa] C_{10} [kPa]					
2A I-block	19.7	17.9	19.2	18.1	
10A I-block 1	28.3	24.6	27.8	26.0	
10A I-block 2	32.5	30.5	31.4	29.8	
20A S-block	133.4	116.9	133.3	121.5	
2A I-block	1.1×10^{-10}	0	0	0	
10A I-block 1	2.2×10^{-10}	0	0	0	
10A I-block 2	1.4×10^{-9}	8.3×10^{-10}	0	0	
20A S-block	0	1.1×10^{-10}	0	5.5×10^{-11}	

For all cases, data are presented without any additional Gaussian blurring. Two choices of virtual field (three simple analytical fields or the full experimentally-measured deformation) and two types of data equalization (dividing the cost function ϕ by the external work at either each global strain, respectively, or the maximum strain) are considered for the Neo-Hookean and second order case. A best fit solution assuming uniaxial tension, using the applied load, MR-derived cross-sectional area over the middle 50%, and the median longitudinal stretch λ_1 per stretch step, is shown (with 95% confidence interval) for comparison of the rectangular I-block samples in the last column

high, any measured volumetric deformation we find is in the noise floor and not actually produced experimentally. There are some interesting trends and comparisons in Table 3. First, the shear moduli found by assuming simple analytical virtual fields and using the measured deformation field are very similar for the same respective data equalization cases, which suggests that the simple test functions are adequate to extract the necessary information from the measured deformation fields to produce precise estimates of $\boldsymbol{\xi}^*$. Secondly, weighting the data by the respective global external work at the sampled step was shown to increase shear modulus estimates, generally creating better agreement with the uniaxial solution. Additionally, the coefficient on the quadratic term C_{20} drops to zero

or nearly zero in all cases, suggesting good agreement with a Neo-Hookean description and processing robustness. Similarly, VFM analysis assuming the eight-chain model [37] produced rubbery moduli C_r identical to the values of C_{10} found in Table 3, while all locking stretches converged either exactly to or within a small distance of the very large upper bound ($\lambda_m \leq 1000$), suggesting a lack of identifiability of λ_m given only the relatively small stretch states tested.

However, upon introduction of a linear term in the second invariant, i.e. the Mooney-Rivlin material model, the $\hat{\phi}$-space profile changes considerably. Specifically, the well-defined least-squares minimum of Fig. 7(b) disappears, replaced by a band of near-minimum in $C_{10} - C_{01}$ space,
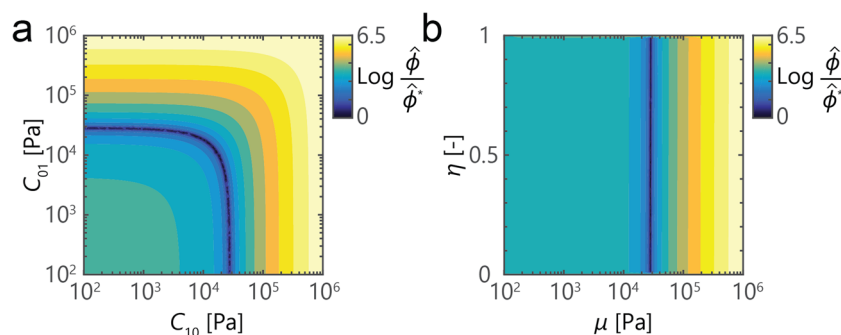
Fig. 10 Cost function space for two forms of the Mooney-Rivlin model. (**a**) Contour plot of the cost function $\hat{\phi}$, normalized by the best fit value $\hat{\phi}^*$ for the first 10A I-block data set. Note that the nearly-uniaxial test is unable to differentiate between the biaxial and uniaxial terms, which results in a minimum band of $\hat{\phi}$, rather than a distinct value. (**b**) A transform of variables into a shear modulus μ and a mixture parameter η clearly highlights the confidence disparity, with the value of μ well defined as a valley but η without obvious minima

as shown in Fig. 10(a). Typically, C_{10} is assumed to be much greater than C_{01} for the Mooney-Rivlin model [46], but in this case the nearly pure uniaxial geometry creates difficulties for differentiation between the two constants. However, a change of variables for the incompressible Mooney-Rivlin strain energy function from $U = C_{10}(\bar{I}_1 - 3) + C_{01}(\bar{I}_2 - 3)$ to $U = \mu(1 - \eta)(\bar{I}_1 - 3) + \mu\eta(\bar{I}_2 - 3)$ highlights the relative identifiability of the shear modulus μ and the mixture parameter η more clearly in Fig. 10(b). Following the method of [10] and extending the complex loading state into 3D may be the path forward, as well as a useful direction for optimization of 3D test geometries for specific constitutive models.

Conclusions

We have incorporated full-field material characterization into a recently published method of magnetic resonance-based method [35] for determining full 3D deformation fields inside compliant materials at native resolutions of approximately 0.5 mm, producing full field volumes of approximately 22,000 points of usable tensor data in approximately 45 minutes. The technique does not rely on native or introduced contrast as in digital correlation or speckle interferometry techniques, as magnetic phase accumulation in a material volume moving between the reference and a deformed configuration is the experimentally measured quantity. The material platform considered herein includes multiple grades of nearly-incompressible silicone rubber, but this method is generally extendable to any material class that has sufficient T_1 signal (including water-containing hydrogels, biological tissues such as ligaments *ex* or *in vivo*, other anhydrous rubbery materials, etc.). Deformation fields acquired were then used for the characterization of materials (MR-*u*) via the VFM, which leverages the principal of virtual work given 3D deformation and global load to inversely solve for material properties. The virtual fields themselves are test functions and should be chosen in such a way that they all contribute to the cost function to extract the various energetic contributions of the spatial deformation field. Material property estimates of rectangular prism "I-block" samples were in good agreement with a uniaxial approximation of the midsection, with the choice of the virtual field as the actual displacement field and equally weighting the effect of each data point providing the closest agreement with the analytical model in general.

With the substantially growing presence of novel uncertainty quantification and machine learning techniques, we believe there are numerous potential improvements and directions forward, particularly in two general areas: (a) improving and robustly quantifying confidence in

material parameters from a range of material models and (b) optimizing the experimental platform (e.g. in the MR calibration procedure, or choosing sample geometries where applicable). Options such as variational system identification [47] and the use of Bayesian inference to incorporate previous experimental results toward assessing new data [48] are attractive future frameworks and directions.

Compliance with Ethical Standards

Appendix A: Divolution

We illustrate our complex division-based numerical gradient approximation technique by the following example. Suppose first that we have an unwrapped scalar phase field $\theta = \text{angle}(Z)$ which is proportional to a single component of our induced displacement field u_k. We can smooth or numerically differentiate θ by convolution, or passing filter kernels w and d, respectively, over it as illustrated in Fig. 5. The phase function θ is defined at every pixel index i and j for the 2D example, which is henceforth denoted as $\theta^{(i,j)}$. By passing a symmetric smoothing filter w in the j direction over $\theta^{(i,j)}$, we produce a smoothed function

$$\bar{\theta}^{(i,j)} = \sum_{n=-H}^{H} w_n \theta^{(i,j+n)}, \tag{13}$$

while by passing an antisymmetric edge filter d (with a middle component of zero) in the j direction, we determine the average central phase difference

$$\overline{\Delta_j \theta}^{(i,j)} = \sum_{n=1}^{H} d_n \left(\theta^{(i,j+n)} - \theta^{(i,j-n)} \right), \tag{14}$$

where $2H + 1$ is the length of the respective filter, and w and d follow normalizations of

$$\sum_{n=-H}^{H} w_n = 1 \text{ and } \sum_{n=1}^{H} d_n = 1 \tag{15}$$

If instead, the phases are wrapped on $(-\pi/2, \pi/2)$, simple convolution operators will produce unwanted phase gradients or smoothing operations at the $\pm\pi/2$ jumps. We can avoid smoothing wrap jumps by using the complex

data Z directly. Notably, the values of Z are independent of the wrapping of θ, making Z itself a usable quantity to minimize unwrapping artifacts. Distinguishing the wrapped phase field $\widetilde{\theta} = \mathrm{wrap}(\theta)$ from its unwrapped counterpart θ, the complex magnetic resonance output field Z at a pixel (i, j) is represented in polar form as

$$Z^{(i,j)} = r^{(i,j)} \exp(i\theta^{(i,j)}) = r^{(i,j)} \exp(i\widetilde{\theta}^{(i,j)}), \quad (16)$$

where $r^{(i,j)}$ represents the magnitude of the image signal. With equation (16), complex division can be used to produce the result of equation (14) in a similar way to a convolution filter - pixels on either side of the filter can be divided by one another, or *divolved*, to subtract phases. The divolution process is illustrated in Fig. 5(d), and the phase gradient can be expressed as

$$\overline{\Delta_j \theta}^{(i,j)} = \mathrm{angle}\left[\prod_{n=1}^{H} \left(\frac{Z^{(i,j+n)}}{Z^{(i,j-n)}} \right)^{d_n} \right]$$
$$= \mathrm{angle}\left[\prod_{n=1}^{H} \frac{r^{(i,j+n)} \exp\left(i d_n \theta^{(i,j+n)}\right)}{r^{(i,j-n)} \exp\left(i d_n \theta^{(i,j-n)}\right)} \right]. \quad (17)$$

Appendix B: Gradient Coil Calibration

Correcting for the non-linearity in the imaging gradient set requires a set of two experiments: (a) a rigid translation of a large block of material to determine the higher order deviations from a linear gradient and (b) a spatial grid of material to determine both local and global dilation along the longitudinal direction, essentially the integration constant from the former. In general, we can describe the unwrapped phase field $\boldsymbol{\theta}(X)$ for a sample in an ideal gradient coil, as in equation (7), as

$$\boldsymbol{\theta}(X) = \frac{\boldsymbol{u}(X)}{\Lambda}, \quad (18)$$

where X is a position in our sample's reference configuration, $\boldsymbol{u}(X)$ is the displacement in the sample, and Λ is the encoding length chosen by the user corresponding to how many phase wraps occur per 2π in the respective direction. However, as real gradient coils are designed to be very close to linear in the central region, the non-linearity at the periphery must be considered for calculating displacements and strains to a high degree of accuracy. We can describe the non-ideal gradient $\boldsymbol{G}'$ with higher-order terms as $\boldsymbol{G}(1 + \alpha(X))$. Given the relation between our encoding length Λ and the applied magnetic field gradient,

$$\Lambda = \frac{1}{\gamma_H t_e \boldsymbol{G}}, \quad (19)$$

we can write the phase in a non-ideal gradient coil as

$$\boldsymbol{\theta}(X) = \frac{\boldsymbol{u}(X)}{\Lambda} (1 + \boldsymbol{\alpha}(X)), \quad (20)$$

where $\boldsymbol{\alpha}$ is the higher order gradient coil correction function which is purely a vector function of the MR coordinate system $\boldsymbol{\chi}$ (with all χ_i parallel to X_i). For cases of rigid translation of amplitude w, we can then rearrange for $\boldsymbol{\alpha}(X)$,

$$\boldsymbol{\alpha}(X) = \frac{\Lambda}{w} (\boldsymbol{\theta}(X) - \boldsymbol{\theta_0}) + C, \quad (21)$$

where $\boldsymbol{\theta_0}$ is the value at the gradient coil center $\boldsymbol{\theta}(\boldsymbol{\chi} = \boldsymbol{0})$, and C is a constant taking into account the possibility of an offset error at the center.

For calibration of our setup, we ran two rigid translation experiments of 5mm and 7.5mm, respectively. As described in Section "Loading and Imaging Procedure", phase maps were put through the processing procedure shown in Fig. 5. Importantly, phase maps were first unwrapped using the procedure described in [41], which prioritizes unwrapping of pixels based on the flatness of the second central difference. Surface fits for the components $\alpha_i(\chi)$ (i.e. using $\theta_i(\chi)$) were then performed to values on symmetric planes in the gradient coil (χ_1-χ_2, χ_1-χ_3). Furthermore, due to symmetry in gradient set design and winding, α_1 is comprised of even terms, while α_2 and α_3 are comprised of odd terms in $\boldsymbol{\chi}$. The expressions α_i were found to be well-described by the analytical forms:

$$\alpha_1 = (n_2\chi_2^2 + C_2)(n_3\chi_3^2 + C_3)$$
$$\times \left[a_1(\chi_1 - e_1)^4 + b_1(\chi_1 - e_1)^2 + d_1 \right] + c_1 \quad (22)$$
$$\alpha_2 = \chi_2 \left[a_2(\chi_1 - e_2)^3 + b_2(\chi_1 - e_2) + d_2 \right] + c_2 \quad (23)$$
$$\alpha_3 = \chi_3 \left[a_3(\chi_1 - e_3)^3 + b_3(\chi_1 - e_3) + d_3 \right] + c_3, \quad (24)$$

where n_i, C_i, a_i, b_i, c_i, d_i, and e_i are all fitting constants.

To correct displacement gradient tensor data in practice, we can take analytical derivatives of the gradient coil correction function $\boldsymbol{\alpha}$ and apply them to components,

$$F'_{ij}(X) = F_{ij}(X) - \frac{\partial \alpha_i}{\partial \chi_j}(X) \cdot u_1(X), \quad (25)$$

where F'_{ij} is the correction of the deformation gradient tensor with components F_{ij}, and $\frac{\partial \alpha_i}{\partial \chi_j}(X) \equiv \alpha_{i,j}(X)$, for completeness, are,

$$\alpha_{1,1} = (n_2\chi_2^2 + C_2)(n_3\chi_3^2 + C_3)$$
$$\times \left[4a_1(\chi_1 - e_1)^3 + 2b_1(\chi_1 - e_1) \right] \quad (26)$$
$$\alpha_{1,2} = 2n_2\chi_2(n_3\chi_3^2 + C_3)$$
$$\times \left[a_1(\chi_1 - e_1)^4 + b_1(\chi_1 - e_1)^2 + d_1 \right] \quad (27)$$

$$\alpha_{1,3} = 2n_3\chi_3(n_2\chi_2^2 + C_2)$$
$$\times \left[a_1(\chi_1 - e_1)^4 + b_1(\chi_1 - e_1)^2 + d_1\right] \quad (28)$$

$$\alpha_{2,1} = \chi_2\left[3a_2(\chi_1 - e_2)^2 + b_2\right] \quad (29)$$

$$\alpha_{2,2} = a_2(\chi_1 - e_2)^3 + b_2(\chi_1 - e_2) + d_2 \quad (30)$$

$$\alpha_{2,3} = 0 \quad (31)$$

$$\alpha_{3,1} = \chi_3\left[3a_2(\chi_1 - e_2)^2 + b_2\right] \quad (32)$$

$$\alpha_{3,2} = 0 \quad (33)$$

$$\alpha_{3,3} = a_3(\chi_1 - e_3)^3 + b_3(\chi_1 - e_3) + d_3. \quad (34)$$

References

1. Pierron F, Grédiac M (2012) The virtual fields method, 1st edn. Springer, New York
2. Pierron F, Grédiac M (2000) Identification of the through-thickness moduli of thick composites from whole-field measurements using the Iosipescu fixture: theory and simulations. Compos Appl Sci Manuf 31(4):309–318
3. Avril S, Pierron F (2007) General framework for the identification of constitutive parameters from full-field measurements in linear elasticity. Int J Solids Struct 44(14-15):4978–5002
4. Grédiac M, Pierron F, Surrel Y (1999) Novel procedure for complete in-plane composite characterization using a single T-shaped specimen. Exp Mech 39(2):142–149
5. Pierron F, Vert G, Burguete R, Avril S, Rotinat R, Wisnom MR (2007) Identification of the orthotropic elastic stiffnesses of composites with the virtual fields method: sensitivity study and experimental validation. Strain 43(3):250–259
6. Xavier J, Avril S, Pierron F, Morais J (2007) Novel experimental approach for longitudinal-radial stiffness characterisation of clear wood by a single test. Holzforschung 61(5):573–581
7. Grédiac M, Pierron F (2006) Applying the virtual fields method to the identification of elasto-plastic constitutive parameters. Int J Plast 22(4):602–627
8. Chalal H, Avril S, Pierron F, Meraghni F (2006) Experimental identification of a nonlinear model for composites using the grid technique coupled to the virtual fields method. Compos Part A Appl Sci Manuf 37(2):315–325
9. Pannier Y, Avril S, Rotinat R, Pierron F (2006) Identification of elasto-plastic constitutive parameters from statically undetermined tests using the virtual fields method. Exp Mech 46(6):735–755
10. Promma N, Raka B, Grédiac M, Toussaint E, Le Cam J-B, Balandraud X, Hild F (2009) Application of the virtual fields method to mechanical characterization of elastomeric materials. Int J Solids Struct 46(3–4):698–715
11. Avril S, Badel P, Duprey A (2010) Anisotropic and hyperelastic identification of in vitro human arteries from full-field optical measurements. J Biomech 43(1):2978–2985
12. Romo A, Badel P, Duprey A, Favre J-P, Avril S (2014) In vitro analysis of localized aneurysm rupture. J Biomech 47(3):607–616
13. Bersi MR, Bellini C, Di Achille P, Humphrey JD, Genovese K, Avril S (2016) Novel methodology for characterizing regional variations in the material properties of murine aortas. J Biomech Eng 138(7)
14. Avril S, Evans S (2017) Material parameter identification and inverse problems in soft tissue biomechanics, 1st edn. Springer, New York
15. Hild F, Roux S (2006) Digital image correlation: from displacement measurement to identification of elastic properties – a review. Strain 42(2):69–80
16. Ri S, Fujigaki M, Morimoto Y (2010) Sampling moiré method for accurate small deformation distribution measurement. Exp Mech 50(4):501–508
17. Pierron F, Zhu H, Siviour C (2014) Beyond Hopkinson's bar. Philos Trans Royal Soc A 372(2023):20130195
18. Fletcher L, van Blitterswyk J, Pierron F (2019) A novel image-based inertial impact test (IBII) for the transverse properties of composites at high strain rates. J Dyn Behav Mater 5(1):65–92
19. Mallett KF, Arruda EM (2017) Digital image correlation-aided mechanical characterization of the anteromedial and posterolateral bundles of the anterior cruciate ligament. Acta Biomater 56:44–57
20. Luetkemeyer CM, Cai L, Neu CP, Arruda EM (2018) Full-volume displacement mapping of anterior cruciate ligament bundles with dualMRI. Extreme Mech Lett 19:7–14
21. Stout DA, Bar-Kochba E, Estrada JB, Toyjanova J, Kesari H, Reichner JS, Franck C (2016) Mean deformation metrics for quantifying 3D cell–matrix interactions without requiring information about matrix material properties. Proc Natl Acad Sci USA 113(11):2898–2903
22. Fu J, Pierron F, Ruiz PD (2013) Elastic stiffness characterization using three-dimensional full-field deformation obtained with optical coherence tomography and digital volume correlation. J Biomed Opt 8(12):121512
23. Gillard F, Boardman R, Mavrogordato M, Hollis D, Sinclair I, Pierron F, Browne M (2014) The application of digital volume correlation (DVC) to study the microstructural behaviour of trabecular bone during compression. J Mech Behav Biomed Mater 29:480–499
24. Bay BK, Smith TS, Fyhrie DP, Saad M (1999) Digital volume correlation: three-dimensional strain mapping using X-ray tomography. Exp Mech 39(3):217–226
25. Midgett DE, Pease ME, Jefferys JL, Patel M, Franck C, Quigley HA, Nguyen TD (2017) The pressure-induced deformation response of the human lamina cribrosa: analysis of regional variations. Acta Biomater 53(15):123–139
26. Stejskal EO, Tanner JE (1965) Spin diffusion measurements: spin echoes in the presence of a time-dependent field gradient. J Chem Phys 42:288–292
27. Aletras AH, Ding S, Balaban RS, Wen H (1999) Dense: displacement encoding with stimulated echoes in cardiac functional MRI. J Magn Reson 137:242–247
28. Neu CP, Walton JH (2008) Displacement encoding for the measurement of cartilage deformation. Magn Reson Med 59(1):149–55
29. Butz KD, Chan DD, Nauman EA, Neu CP (2011) Stress distributions and material properties determined in articular cartilage from MRI-based finite strains. J Biomech 44(15):2667–72
30. Pierce DM, Ricken T, Neu CP (2018) Image-driven constitutive modeling for FE-based simulation of soft tissue biomechanics. Book Chapter, numerical methods and advanced simulation in biomechanics and biological processes. Academic Press, London
31. Osman NF, Kerwin WS, McVeigh ER, Prince JL (1999) Cardiac motion tracking using CINE harmonic phase (HARP) magnetic resonance imaging. Magn Reson Med 42(6):1048–60
32. Sampath S, Osman NF, Prince JL (2009) A combined harmonic phase and strain-encoded pulse sequence for measuring three-dimensional strain. Magn Reson Imaging 27(1):55–61
33. Sabet AA, Christoforou E, Zatlin B, Genin GM, Bayly PV (2008) Deformation of the human brain induced by mild angular head acceleration. J Biomech 41(2):307–315

34. Bayly PV, Clayton EH, Genin GM (2012) Quantitative imaging methods for the development and validation of brain biomechanics models. Annu Rev Biomed Eng 14:369–396

35. Scheven UM, Estrada JB, Luetkemeyer CM, Arruda EM (2020) Robust high resolution strain imaging by alternating pulsed field gradient stimulated echo imaging (APGSTEi) at 7 Tesla. J Magn Reson 310:106620

36. Mariappan YK, Glaser KJ, Ehman RL (2010) Magnetic resonance elastography: a review. Clin Anat 23(5):497–511

37. Arruda EM, Boyce MC (1993) A three-dimensional constitutive model for the large stretch behavior of rubber elastic materials. J Mech Phys Solids 41(2):389–412

38. Connesson N, Clayton EH, Bayly PV, Pierron F (2015) Extension of the optimized virtual fields method to estimate viscoelastic material parameters from 3D dynamic displacement fields. Strain 51(2):110–134

39. Marek A, Davis FM, Rossi M, Pierron F (2019) Extension of the sensitivity-based virtual fields to large deformation anisotropic plasticity. Int J Mater Form 12(3):457–476

40. Cotts RM, Hoch MJR, Sun T, Markert JT (1989) Pulsed field gradient stimulated echo methods for improved NMR diffusion measurements in heterogeneous systems. J Magn Res 83:252–266

41. Abdul-Rahman HS, Gdeisat MA, Burton DR, Lalor MJ, Lilley F, Moore CJ (2007) Fast and robust three-dimensional best path phase unwrapping algorithm. Appl Opt 46:6623–6635

42. Jenkinson M (2003) Fast, automated, N-dimensional phase-unwrapping algorithm. Magn Reson Med 49(1):193–197

43. International Digital Image Correlation Society, Jones EMC, Iadicola MA (eds.) (2018) A good practices guide for digital image correlation. https://doi.org/10.32720/idics/gpg.ed1

44. Markl M, Bammer R, Alley MT, Elkins CJ, Draney MT, Barnett A, Moseley ME, Glover GH, Pelc NJ (2003) Generalized reconstruction of phase contrast MRI: analysis and correction of the effect of gradient field distortions. Mag Reson Med 50:791–801

45. Nelder JA, Mead R (1965) A simplex method for function minimization. Comput J 7:308–313

46. Bower AF (2009) Applied mechanics of solids, 1st edn. CRC Press, Boca Raton

47. Wang Z, Huan X, Garikipati K (2019) Variational system identification of the partial differential equations governing the physics of pattern-formation: inference under varying fidelity and noise. Comput Methods Appl Mech Engrg 356: 44–74

48. Huan X, Marzouk YM (2013) Simulation-based optimal Bayesian experimental design for nonlinear systems. J Comput Phys 232(1):288–317